

Successive ferroelectric orders and magnetoelectric coupling without long-range magnetic order in highly frustrated pyrochlore compounds: $\text{Sm}_2\text{Ti}_{2-x}\text{V}_x\text{O}_7$

S. Mukherjee¹, O. Ivashko², S. Majumdar¹, A. Kumar³, and S. Giri^{1*}

¹*School of Physical Sciences, Indian Association for the Cultivation of Science, Jadavpur, Kolkata 700032, India*

²*Deutsches Elektronen-Synchrotron DESY Notkestr. 85, 22607 Hamburg, Germany and*

³*Solid State Physics Division, Bhabha Atomic Research Centre, Mumbai 400085, India and Homi Bhabha National Institute, Anushaktinagar, Mumbai 400094, India*

$\text{Sm}_2\text{Ti}_2\text{O}_7$, a member of rare-earth titanate pyrochlores, exhibits dipolar-octupolar antiferromagnetism below $T_N = 0.35$ K. We observed two ferroelectric transitions at 182 (T_{FE1}) and 52 K (T_{FE2}), significantly higher than T_N for $\text{Sm}_2\text{Ti}_{2-x}\text{V}_x\text{O}_7$ ($x = 0, 0.1$). Although the ferroelectric transition temperatures remain unchanged, the polarization value decreases considerably with V doping. A structural transition to a polar $R3m$ rhombohedral phase from the cubic $Fd\bar{3}m$ structure occurs at T_{FE1} , involving a distortion in the pyrochlore lattice. Remarkably, significant linear magnetoelectric coupling is observed in both compounds, with further enhancement of magnetoelectric coupling due to magnetic V doping. The existence of magnetoelectric coupling without long-range magnetic order in a frustrated pyrochlore system could enable the tailoring of magnetoelectric coupling properties, which can be further fine-tuned through V doping. The emergence of ferroelectricity in a frustrated magnetic system introduces an intriguing aspect to these compounds and paves the way for developing ferroelectric order driven by the alleviation of magnetic frustration in pyrochlore systems.

I. INTRODUCTION

The frustrated pyrochlore structure, manifesting in compounds with the chemical formula $R_2B_2O_7$ [1] (R = Rare earth elements; $M = \text{Zr, Hf, Ti, Sn, Pb}$), stands as a captivating archetype in the realm of condensed matter physics and materials science. This structure, defined by a lattice of corner-sharing tetrahedra formed by R cations interconnected by oxygen ions, embodies a symphony of competing interactions and geometric frustrations. The delicate interplay between the magnetic frustration inherent in the pyrochlore lattice and the magnetic exchange interactions often gives rise to a plethora of exotic physical phenomena, spanning from unconventional magnetic ground states to intriguing electronic behaviors. Within the domain of magnetism, frustrated pyrochlores have garnered significant attention due to their propensity to host intriguing magnetic phases such as spin liquids [2, 3], spin ice [4–6], and spin glasses [7, 8].

The pyrochlore family, represented by the chemical formula $R_2\text{Ti}_2\text{O}_7$ (where R ranges from Gd to Yb), is renowned for being exemplary three-dimensional geometrically frustrated systems [9]. This recognition stems from their intriguing and unconventional magnetic characteristics. Within these insulating pyrochlore structure, a variety of rich characteristic features have been witnessed. These include suppressed moment in $\text{Gd}_2\text{Ti}_2\text{O}_7$ [10, 11], single-ion anisotropy of Tb^{3+} within the collective paramagnetic-spin liquid state in $\text{Gd}_2\text{Ti}_2\text{O}_7$ [12, 13], and the realization of quantum order by disorder and accidental soft mode in $\text{Er}_2\text{Ti}_2\text{O}_7$ [14, 15]. On the other hand, intriguing magnetic behavior from spin ice

state to supercooled spin liquid state has been observed in $\text{Dy}_2\text{Ti}_2\text{O}_7$ [16, 17], the emergence of magnetic monopoles has been noted in $\text{Gd}_2\text{Ti}_2\text{O}_7$ [18–20], and evidence of quantum spin-liquid behavior has been found in $\text{Yb}_2\text{Ti}_2\text{O}_7$ [21, 22].

Magnetism of our focal compound, $\text{Sm}_2\text{Ti}_2\text{O}_7$, as a member of pyrochlore $R_2\text{Ti}_2\text{O}_7$ family, has been relatively underexplored at the microscopic level, particularly through neutron scattering. This is due to the fact that ^{149}Sm is a strong neutron absorber. Nevertheless, recent neutron scattering, facilitated by enriching the ^{154}Sm isotope, and muon relaxation studies have revealed that the compound exhibits the all-in, all-out magnetic structure with an ordered moment of $0.44(7)\mu_B$ below $T_N = 0.35$ K. This observation aligns with expectations for antiferromagnetically coupled Ising spins on the pyrochlore lattice [23, 24]. Consistent with this findings, bulk magnetization studies do not indicate long range magnetic order down to 0.5 K. This absence was attributed to weak exchange (Curie-Weiss temperature ~ -0.26 K) and dipolar interactions ($\mu_{eff} \sim 0.15 \mu_B$)

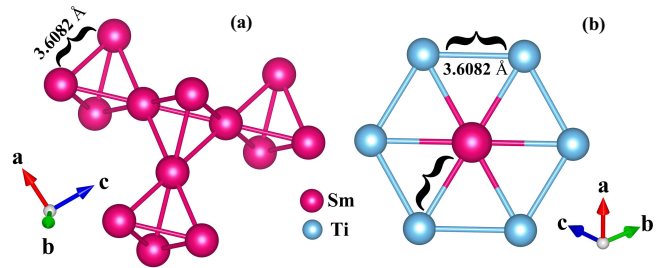


FIG. 1. (a) Equidistant pyrochlore structure of STO formed by Sm atoms and (b) formation of an equidistant hexagonal structure by Ti atoms, with Sm atoms sitting at the center.

* Corresponding author: sspsg2@iacs.res.in

between the Sm^{3+} spins within this pyrochlore structure [25].

Recent developments suggest the potential occurrence of ferroelectric (FE) order in the pyrochlore $R_2\text{Ti}_2\text{O}_7$ family, where $R = \text{La}, \text{Ce}, \text{Pr}, \text{and Nd}$, based on first-principles studies utilizing density functional theory [27]. While the search for FE order has rarely been attempted in polycrystalline materials [28, 29] and films [30, 31], we are motivated to explore FE order as well as magnetoelectric coupling in $\text{Sm}_2\text{Ti}_{2-x}\text{V}_x\text{O}_7$ ($x = 0, 0.1$), members of this pyrochlore family. In line with previous findings, Fig. 1(a) depicts the characteristic pyrochlore structure of $\text{Sm}_2\text{Ti}_2\text{O}_7$, wherein all vertices of a regular tetrahedron are equidistant from each other, measuring a length of 3.6082 \AA at 300 K, as obtained from Rietveld refinement (Fig. 2(a)). Figure 1(b) illustrates the formation of an equidistant (3.6082 \AA) hexagonal structure by Ti atoms, with magnetic Sm^{3+} occupying the center. Notably, Ti atoms form Edge-sharing equilateral triangles, with the Sm atom positioned at the common vertices. Now, if we replace the Ti^{4+} ion with magnetic V^{4+} , the magnetic V^{4+} ions, arranged in an equilateral triangle, influence frustrated magnetism due to the pyrochlore structure formed by Sm^{3+} ions and act as a perturbation to the frustrated magnetism of $\text{Sm}_2\text{Ti}_2\text{O}_7$.

In this article, we present findings on FE order accompanied by a structural transition to a polar $R3m$ structure from the cubic $Fd\bar{3}m$ structure. Of particular significance is the observation of magnetoelectric (ME) coupling in the absence of long-range magnetic order, a phenomenon further amplified by V doping. We discuss the influence of structural distortion and potential short-range effects driven by V doping on the ME coupling.

II. EXPERIMENTAL DETAILS

Polycrystalline $\text{Sm}_2\text{Ti}_2\text{O}_7$ (STO) and $\text{Sm}_2\text{Ti}_{1.9}\text{V}_{0.1}\text{O}_7$ (STVO) were synthesized using a standard solid-state reaction technique. Stoichiometric amounts of Sm_2O_3 and TiO_2 and V_2O_5 (for STVO) were finely ground and thoroughly mixed for several hours. This mixture was first preheated at 500°C for 5 hours. Subsequently, the mixtures were ground and thoroughly mixed before undergoing a final heat treatment at 1300°C for 24 hours after being pressed into pellets [32].

The single-phase chemical compositions were verified using standard X-ray diffraction (XRD) studies at 300 K using a PANalytical X-ray diffractometer (Model: X'Pert PRO) with $\text{Cu-K}\alpha$ radiation. Low-temperature synchrotron X-ray diffraction studies were carried out in the range of 10-300 K using a wavelength, $\lambda = 0.1123 \text{ \AA}$ at P21.1 beam line at DESY, Hamburg, Germany. The diffraction patterns were analyzed using the Rietveld refinement with a commercially available open-source software MAUD (Material Analysis Using Diffraction). Properly prepared pelletized samples were used for the pyroelectric measurements, electrical contacts made us-

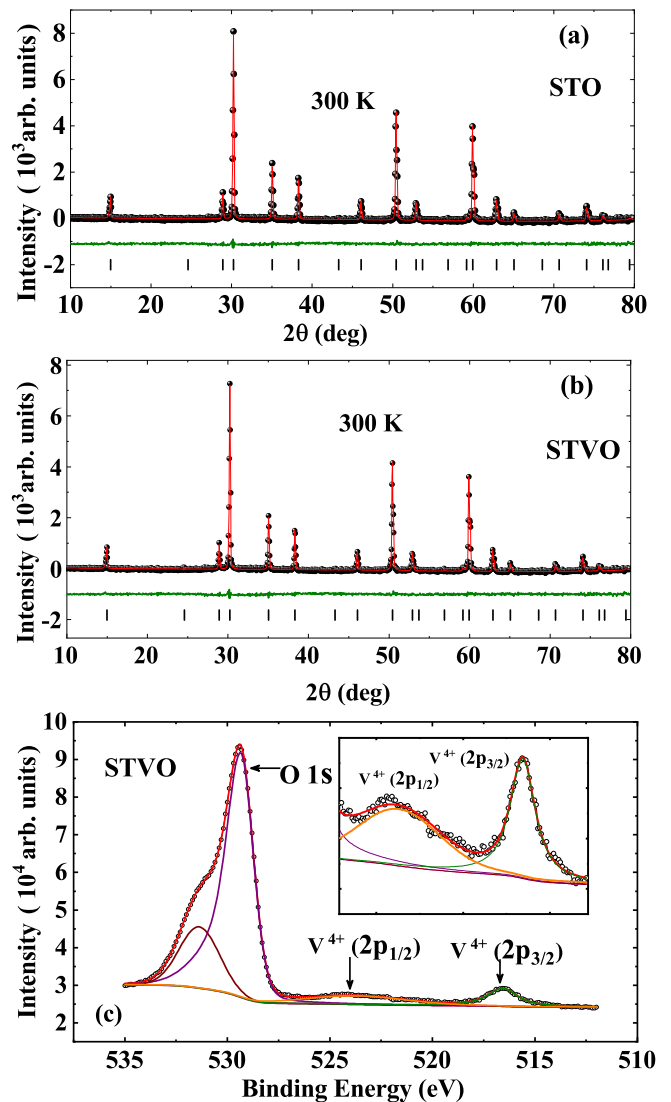


FIG. 2. Rietveld refined XRD patterns at 300 K of (a) STO and (b) STVO. (c) XPS spectrum of STVO. Inset shows deconvolution of (solid curve) of $2p_{1/2}$ and $2p_{3/2}$ spectrum of V^{4+} for STVO.

ing silver paint. Pyroelectric current (I_p) was recorded in constant temperature sweep and magnetic field sweep rates using an electrometer (Keithley, model 6517B) connected to a commercial PPMS-II, EverCool system of Quantum Design. Poling electric fields were applied during the cooling process, and at the lowest temperature, the pellet was properly short-circuited before measuring I_p during the heating process. Similarly, dielectric measurements were performed using an Agilent E4890A LCR meter connected with the same PPMS-II. Magnetization was measured using a commercial magnetometer of Quantum Design (MPMS, EverCool). X-ray photoemission spectroscopy (XPS) was recorded with a spectrometer of Omicron Nanotechnology.

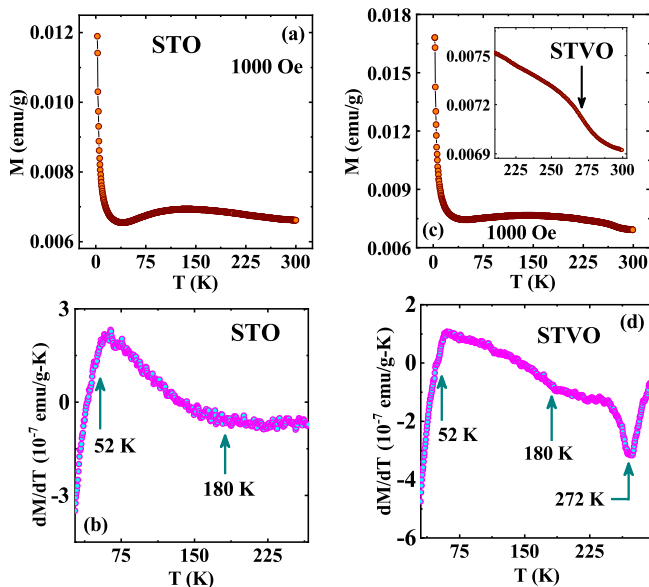


FIG. 3. (a) Thermal (T) variations of magnetization (M) recorded with 1000 Oe for (a) STO and (c) STVO. T variations of dM/dT for (b) STO and (d) STVO. Inset of (c) highlights an anomaly, as indicated by an arrow.

III. EXPERIMENTAL RESULTS AND DISCUSSIONS

The XRD patterns at 300 K of STO and STVO are depicted in Figs. 2(a) and 2(b), respectively. These compounds crystallize in $Fd\bar{3}m$ space group, and Rietveld calculated XRD patterns are represented by the continuous curves in the figures. The goodness of fits for STO and STVO is satisfactory, confirming the absence of any impurity phase, as indicated by the difference plotted below. The Wyckoff positions for STO are as follows: Sm(0.5000, 0.5000, 0.5000), Ti(0, 0, 0), O1(0.3270(6), 0.1250, 0.1250), O2(0.3750, 0.3750, 0.3750), with a lattice constant, $a = 10.2815(3)$ Å. The reliability parameters are $R_w(\%) \sim 3.47$, $R_{exp}(\%) \sim 1.41$, $\chi^2 \sim 1.56$. The lattice constant at 300 K is close to the reported value for STO [26]. Here, all the Wyckoff positions are fixed except for x for O1. The refined x coordinate for STVO is 0.3272(6). For STVO, the refined lattice constant is $a = 10.2785(6)$ Å, with reliability parameters $R_w(\%) \sim 3.04$, $R_{exp}(\%) \sim 1.78$, $\chi^2 \sim 1.71$. In line with the smaller crystal radius of six-coordinated V^{4+} compared to Ti^{4+} , the lattice constant contracts upon V doping. To identify the oxidation state of V, XPS was recorded for STVO, as shown in Fig. 2(c). Satisfactory fits of the peaks are demonstrated by the continuous curves in the figure. The two peaks located at 524 and 516 eV indicate V^{4+} states of $2p_{1/2}$ and $2p_{3/2}$, respectively, consistent with a previous report [35], confirming the presence of V^{4+} replacing Ti^{4+} .

Temperature-dependent magnetization (M) recorded in zero-field-cooled (ZFC) mode for STO and STVO is

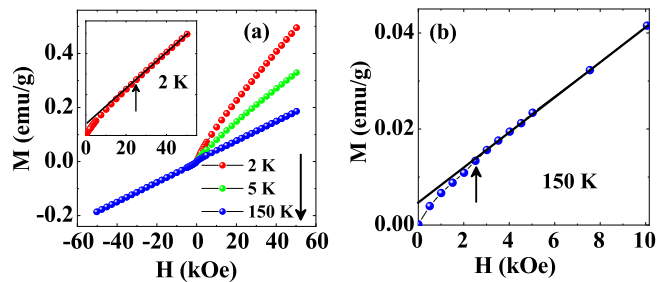


FIG. 4. (a) Isothermal magnetization of STVO at selected T . Inset of (a), and (b) show linear dependence of magnetic field (H) in the high- H regions at 2 and 150 K, respectively.

illustrated in Figs. 3(a) and 3(c), respectively. In the ZFC mode, samples were cooled in zero-field, and magnetization was recorded in the warming mode with $H = 1$ kOe. Broad maxima in $M(T)$ are observed around 150 K for both samples, with a sharp rise observed below ~ 35 K, consistent with a previous report on STO [25]. The broad maximum in STO was attributed to the crystal field effect of Sm^{3+} [25]. For STVO, a new broadened anomaly appears around 270 K, as highlighted in the inset of Fig. 3(c), which emerges due to 5% V doping. Plots of dM/dT with T are depicted in Figs. 3(b) and 3(d), respectively, highlighting prominent characteristic features by the arrows for STO and STVO. The change

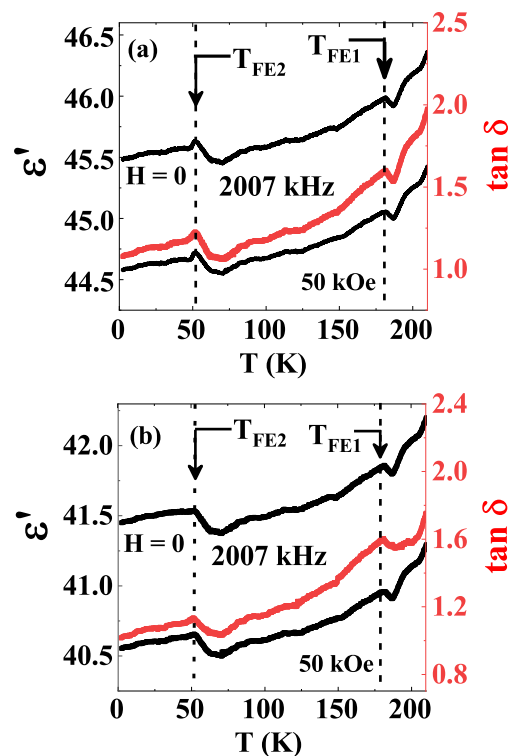


FIG. 5. T variations of real part of dielectric constant (ϵ') at $H = 0$ and 50 kOe, and dielectric loss ($\tan \delta$) at $H = 0$ for (a) STO and (b) STVO, respectively.

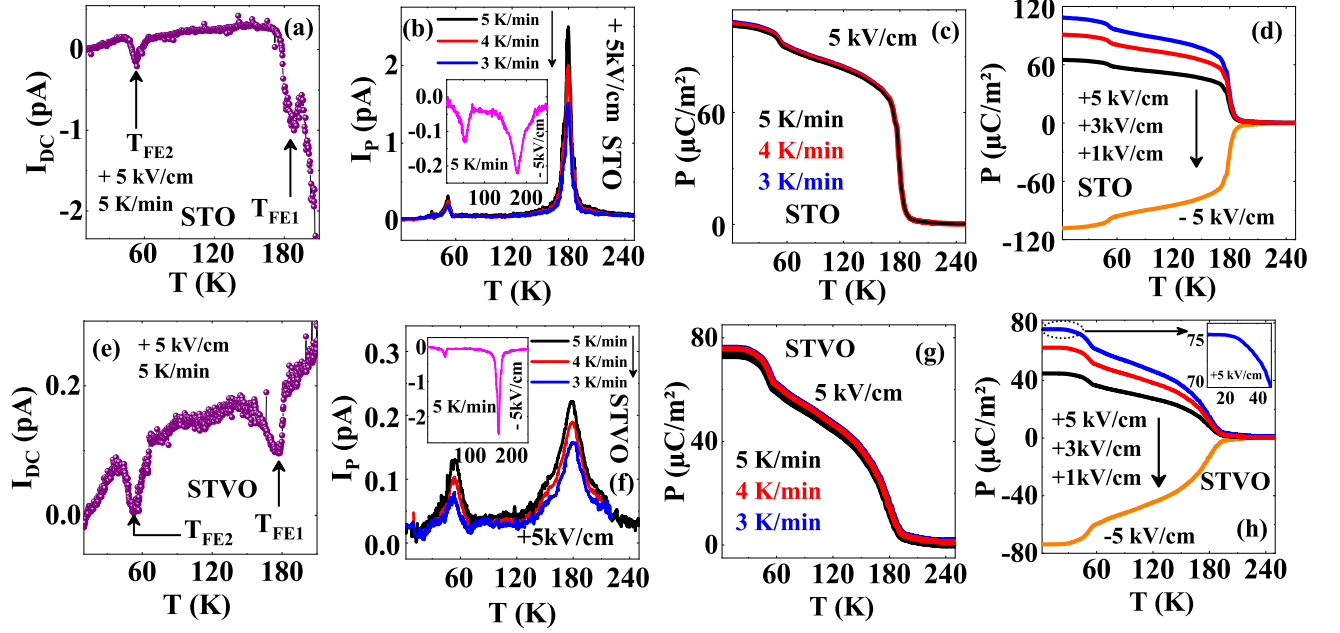


FIG. 6. T variations of I_{DC} for (a) STO and (e) STVO, I_P for different thermal sweep rates for (b) STO and (f) STVO, polarization (P) for different thermal sweep rates for (c) STO and (g) STVO, P at different electric fields for (d) STO and (h) STVO, respectively. Insets of (b) and (f) show I_P for -5kV/cm poling field. Inset of (h) highlights saturating P -value below T_{FE2} for STVO.

of slope in $dM/dT(T)$ around 180 K and an anomaly around 52 K for both STVO and STO, are significant. Because these signatures coincide with the ferroelectric transitions at 52 and 180 K, as discussed elsewhere, indicating magnetoelectric coupling. Additionally, a sharp minimum is observed at 272 K for STVO, likely due to short-range magnetic order attributed to the 5% V doping. The probable short-range ordering in STVO requires further confirmation using other experimental methods. The isothermal magnetization curves of STVO are depicted in Fig. 4(a) at selected T . Unlike the linear behavior of the magnetization curves for STO [25], non-linearity in the magnetization curves is evident at low H for STVO, as highlighted in the inset of Fig. 4(a) at 2 K and 4(b) at 150 K. Arrows in the figures indicate magnetic field, beyond which linearity of the magnetization curves is observed, decrease with increasing T . This non-linearity may correlate with the emergence of a short-range magnetic order below 270 K for STVO.

The dielectric permittivity (ϵ) of STO and STVO were recorded from 2 K to 300 K, for example, at a frequency, $f = 2007$ Hz, under zero-field and with $H = 50$ kOe. Thermal variations of the real component (ϵ') and the dielectric loss ($\tan\delta$) are depicted for STO and STVO in Figs. 5(a) and 5(b), respectively. The $\epsilon'(T)$ and $\tan\delta(T)$ show anomalies at 180 (T_{FE1}) and 52 K (T_{FE2}) for both the compounds. Observing anomalies in $\epsilon'(T)$ and $\tan\delta(T)$ at the same temperature primarily indicates the onset of spontaneous polar order [37, 38]. In the presence of a 50 kOe magnetic field, $\epsilon'(T)$ decrease for both compounds, indicating magneto-dielectric (MD)

response. The percentages of MD responses, defined as $\epsilon'(H)/\epsilon'(H=0) - 1$ at 2 K are 2.1% and 2.4% for STO and STVO, respectively and are consistent with the previous reports [34, 37].

The confirmation of polar order was achieved through various techniques. Upon cooling the sample to its lowest temperature in zero electric field, the bias electric current (I_{DC}) was recorded in the presence of a bias electric field of 5 kV/cm, at a rate of 5 K/min in the warming mode [33]. As depicted in Figs. 6(a) and 6(e), anomalies are evident at 52 and 180 K, indicating the onset of long-range polar order for STO and STVO, respectively, consistent with previous reports [33, 34, 36]. Further, The pyroelectric current (I_P) was recorded under different conditions, such as varied temperature-sweeping rates and different poling electric fields (E), including E reversal, as depicted in Figs. 6(b-d) and 6(f-h). The peak positions at 52 K and 180 K remain unchanged in these measurements, indicating genuine polar orderings for both the compounds. We observe a reduction in the I_P -value with a decrease in temperature-sweeping rate, as depicted in Figs. 6(b) and 6(f) for STO and STVO, respectively. The insets of these figures illustrate $I_P(T)$ at a sweep rate of 5 K/min for a negative poling field of -5 kV/cm. Reversing of $I_P(T)$ confirms ferroelectric order. Integrating $I_P(T)$ over time yields electric polarization (P) using the equation $P = \int I_P dt$. The $P(T)$ curves for STO and STVO are shown in Figs. 6(c) and (g) respectively, for different sweep rates. No significant deviation in $P(T)$ is observed across different sweep rates, indicating the absence of extrinsic contributions from thermally

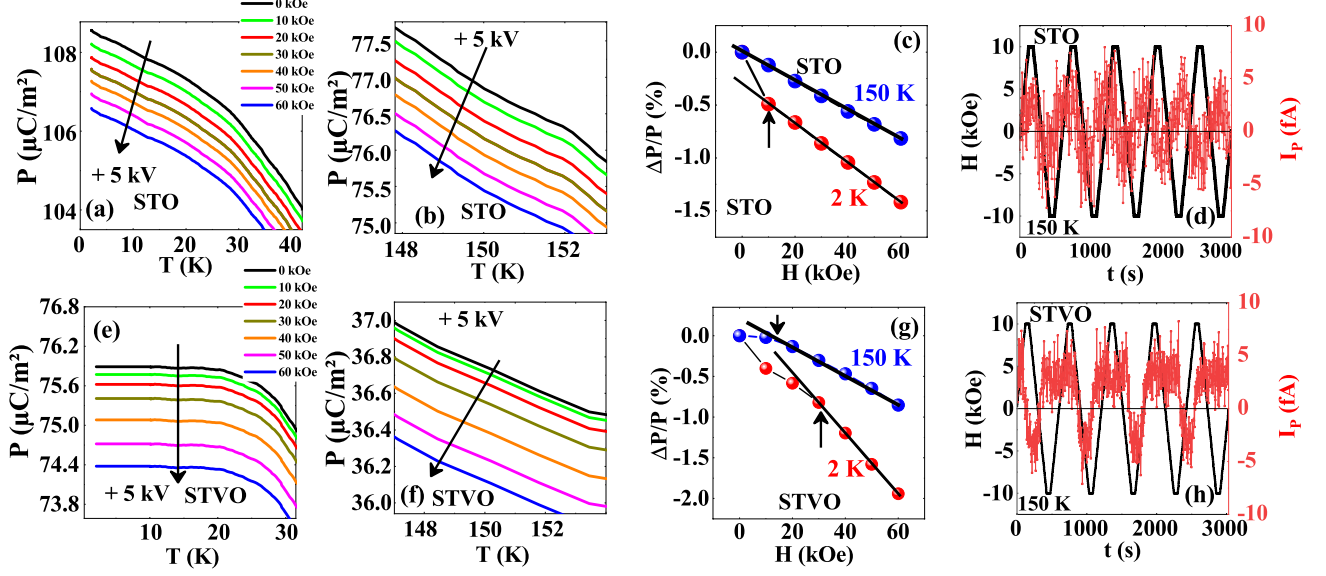


FIG. 7. T variations of magnified polarization (P) under different magnetic fields (H) below T_{FE2} for (a) STO and (e) STVO, and below T_{FE1} for (b) STO and (f) STVO, respectively. H variations of $\Delta P/P$ at 2 and 150 K for (c) STO and (g) STVO, respectively. Time (t) dependent oscillations in H and corresponding I_P at 150 K for (d) STO and (h) STVO, respectively.

stimulated depolarization current (TSDC) [36]. Additionally, we measured $P(T)$ at different poling fields of 5, 3, and 1 kV/cm, as shown in Figs. 6(d) and 6(h). The saturating P -values for STO and STVO are ~ 108 and $\sim 75 \mu\text{C}/\text{m}^2$ respectively, comparable to values for promising multiferroics. [37, 39, 40]. While the transition temperatures T_{FE1} and T_{FE2} remain unchanged, a decrease in $P(T)$ is observed with V doping in STVO, consistent with prior findings regarding the effects of doping [41, 42]. The changes in $P(T)$ at T_{FE1} smears out due to V doping for STVO. In contrast to the behavior observed around T_{FE1} , the increase in $P(T)$ at T_{FE2} is more pronounced and abrupt for STVO compared to STO. Although a slight upward trend in $P(T)$ is observed below T_{FE2} down to the lowest recorded temperature for STO, $P(T)$ stabilizes and remains almost constant below ~ 20 K for STVO, as shown in the inset of Fig. 6(h).

To investigate the manifestation of ME coupling, the polarization was recorded under various applied magnetic field conditions. The $P(T)$ values at selected H are highlighted for STO and STVO in Figs. 7(a) and 7(e), respectively in the low- T region below T_{FE2} , with a poling field of 5 kV/cm. Correspondingly, Figs. 7(b) and 7(f) illustrate the same for the high-temperature range below T_{FE1} . The percentage changes in polarization ($\Delta P/P$), calculated as $[P(H) - P(H = 0)]/P(H = 0) \times 100$, are plotted against H at 2 K (representative temperature below T_{FE2}) and 150 K (representative temperature below T_{FE1}) in Figs. 7(c) and 7(g) for STO and STVO, respectively. It is observed that the decrease in $\Delta P/P$ at 2 K surpasses that at 150 K, indicating stronger ME coupling below T_{FE2} for both the cases. A linear decrease of the $P - H$ curves is noted in the high- H region for

both STO and STVO. The curve remains linear at 150 K and extends into linearity for STO above above 10 kOe. Similarly, for STVO, the $P - H$ curve exhibits linearity above ~ 12 kOe at 150 K and ~ 25 kOe 2 K. Since the initial observation of the linear ME effect in Cr_2O_3 in the 1960s [43, 44], the pursuit of single-phase ME materials demonstrating linear ME coupling has been highly sought after. Recently, linear ME coupling has been identified in LiFePO_4 and $\text{LiNi}_{0.8}\text{Fe}_{0.2}\text{P}_4$ [45], $\text{Na}_2\text{Co}_2\text{TeO}_6$ [34], $\text{Co}_3\text{V}_2\text{O}_8$ [37], and $\text{Gd}_2\text{MnFeO}_6$ [46]. Additionally, it is noted that the values of $\Delta P/P$ are $\sim 1.5\%$ and $\sim 2\%$ under 60 kOe and at 2 K for STO and STVO, respectively. An enhancement of ME is observed due to V doping, albeit with a considerable reduction in the P -value.

The time-dependent behavior of ME was additionally monitored at 150 K for both STO and STVO. In this measurement, sample was initially polarized with an electric field of 5 kV/cm down to 2 K. Subsequently, the electric field was withdrawn, and the sample was properly short-circuited. The sample temperature was then raised to 150 K. The magnetic field was varied between ± 10 kOe with a sweep rate of 100 Oe/s, while simultaneously recording the I_P over time (t), as depicted in Figs. 7(d) and 7(h). For STO, the $I_P(t)$ oscillates approximately between ± 5 fA, exhibiting a phase shift compared to the oscillation of the magnetic field. The value of $I_P(t)$ is small, but it is reproducible and beyond the current measurement resolution of the electrometer. Conversely, the nature of $I_P(t)$ for STVO differs from that of STO. Unlike the regular oscillation $I_P(t)$ for STO, the positive cycle of $I_P(t)$ remains nearly flat and extends over a longer time period compared to sharp change in the negative cycle of $I_P(t)$.

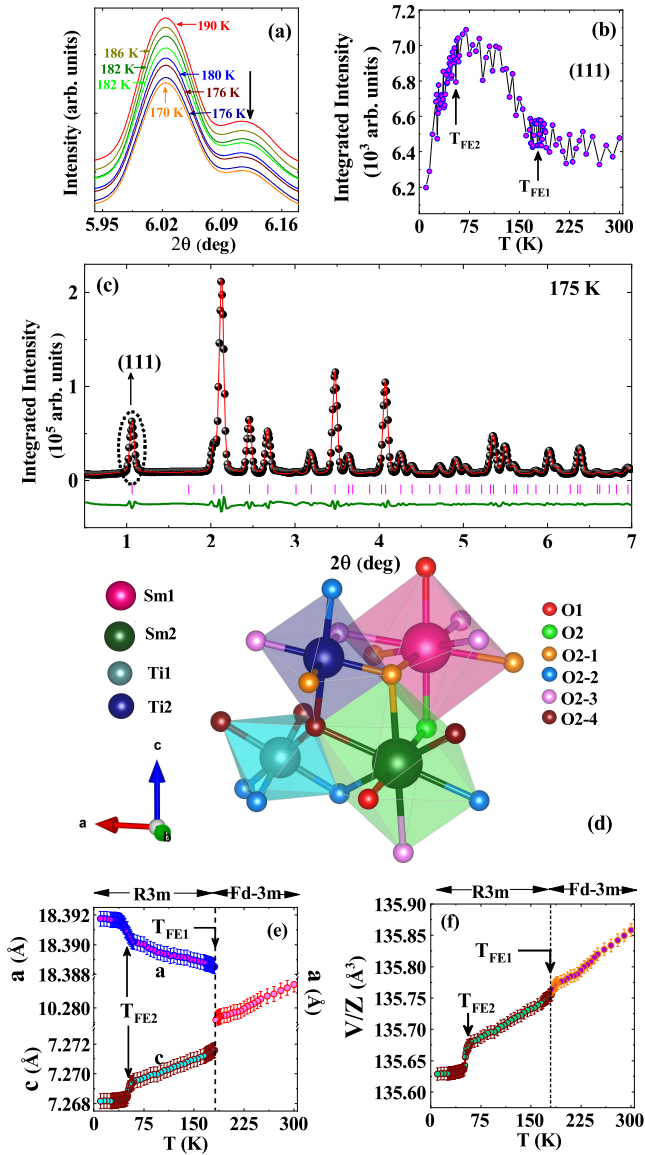


FIG. 8. (a) Selected diffraction peaks at different T around T_{FE1} . (b) T variation of the integrated intensity of (111) peak. (c) Rietveld refinement of synchrotron diffraction pattern at 175 K. The (111) peak is highlighted by a circle. (d) Connecting Sm-polyhedra and Ti-octahedra below T_{FE1} . T variations of lattice parameters (e) a and c , and (f) unit cell volume (V/Z) for STO, where Z is the number of formula unit within the unit cell.

The low-temperature synchrotron diffraction experiments were conducted within the temperature range of 10-300 K for STO. In Figure 8(a), a narrow 2θ region of the diffraction pattern is highlighted around T_{FE1} at selected T , with a 4 K interval. While changes in the intensity of the prominent peak are not readily discernible, subtle variations in the intensity of the smaller peak, indicated by an arrow, are faintly observed, with a notable increase in peak height around T_{FE1} at 180 K. The integrated intensity of the (111) peak, high-

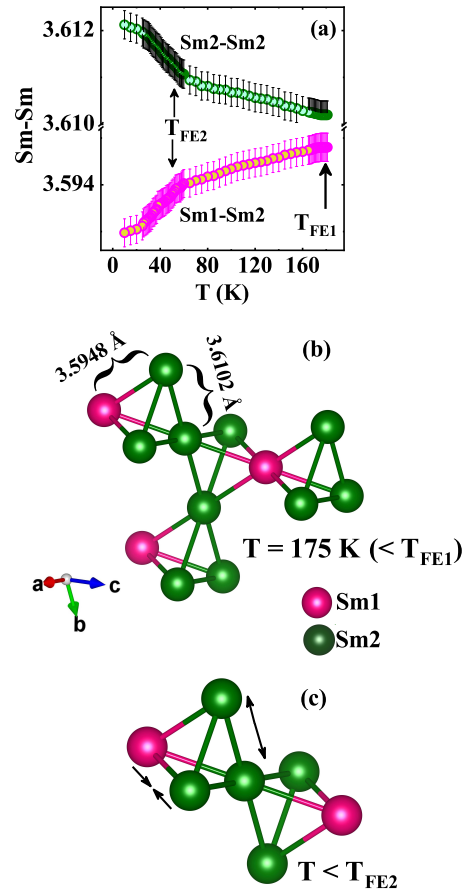


FIG. 9. (a) Sm2–Sm2 and Sm1–Sm2 distances with T below T_{FE1} . Schematic representations of distortion of pyrochlore structure below (b) T_{FE1} and (c) T_{FE2} .

lighted in Fig. 8(c), is shown in Fig. 8(b). The plot indicates a consistent intensity from higher temperatures until T_{FE1} , below which it begins to rise quite sharply, reaching a peak around 75 K before declining below T_{FE2} . The observed changes in integrated intensity around T_{FE1} resemble those observed in multiferroics, suggesting potential structural transitions, including isostructural changes [47, 48] and transitions to the lower symmetries [37, 39, 49, 50]. No additional diffraction peaks were detected below T_{FE1} . However, refinement of the diffraction pattern below T_{FE1} using the room temperature $Fd\bar{3}m$ space group yielded unsatisfactory results, implying a probable structural transition.

We utilize the open-source web software ISODISTORT [52] to discern potential structures at low temperatures. Our analysis reveals that $R3m$ (no. 227) represents a polar structure, exhibiting the highest symmetry among the various structures considered. This finding aligns with the rhombohedral distortion-driven structural transition to $R3m$ structure from $Fd\bar{3}m$, which was associated with the observed FE order in $ZnFe_2O_4$ [51]. A satisfactory Rietveld refinement of the diffraction pattern at 175 K, employing the $R3m$

space group, is presented in Fig. 8(c). The various Wyckoff positions are as follows: Sm1(0,0,0), Sm2(0.50,0,0), Ti1(0,0,0), Ti2(0.833333,0.166667,0.166667), O1(0, 0, 0.625), O2(0, 0, 0.375), O2-1(0.532000, 0.468000, 0.141000), O2-2(0.801330, 0.198670, 0.275670), O2-3(0.134670, 0.865330, 0.192330), O2-4(0.865330, 0.134670, 0.057670). This refinement identifies two Sm, two Ti, and six oxygen atoms within the structure. The connectivity of Sm-polyhedra and Ti-octahedra formed by oxygen atoms is illustrated in Fig. 8(d). The thermal variations of lattice parameters, a and c , and unit cell volume (V/Z), as obtained from the refinement, are depicted in Figs. 8(e) and 8(f), respectively, where Z is the number of formula unit within the unit cell. Besides the structural changes at T_{FE1} , the lattice parameters and the volume show another iso-structural transition near T_{FE2} .

The pyrochlore structure in the $R3m$ phase comprises two Sm atoms, denoted as Sm1 and Sm2. Figure 9(a) shows temperature variations of the Sm2–Sm2 and Sm1–Sm2 distances below T_{FE1} . As temperature decreases, the Sm2–Sm2 distance increases, while the Sm1–Sm2 distance decreases. Figure 9(b) demonstrates that the direct distance between Sm1 and Sm2 is smaller than the Sm2–Sm2 distance, indicating a distortion in the pyrochlore structure. It is significant to note that the equidistant pyrochlore structure formed by Sm atoms at high temperatures, exhibiting the $Fd\bar{3}m$ structure as depicted in Fig. 1, leads to significant magnetic frustration, which becomes distorted following the structural transition at T_{FE1} . We propose that the release of magnetic frustration is a consequence of the structural transition and highlights its pivotal role in the occurrence of ferroelectric order. Evidence supporting the release of magnetic frustration has been observed through an iso-structural transition in the widely studied $\text{CaBaCo}_4\text{O}_7$ [53, 54], resulting in the ferroelectric order. Additionally, in ZnFe_2O_4 , a structural transition from a cubic structure to a lower symmetry of $R3m$ structure is observed to release magnetic frustration and facilitates the occurrence of ferroelectric order. The release of geometric magnetic frustration, attributed to the antiferromagnetic exchange-coupled pyrochlore structure, strongly correlates with this structural transition [51]. Furthermore, it is noteworthy that the structural change at T_{FE1} in STO bears a resemblance to the well-studied multiferroic BiFeO_3 , where the $R3m$ structure induces a rhombohedral distortion of the cubic high-temperature perovskite structure formed by the Bi atoms. This structural distortion is closely associated with the emergence of ferroelectric order in BiFeO_3 [55, 56]. The emergence of ferroelectric order in the presence of magnetic frustration adds a compelling layer of complexity to these materials, rendering them highly intriguing subjects for further scientific exploration. In Fig. 9(a), the significant changes in slope of Sm–Sm distances are observed below T_{FE2} , indicating another distortion in the pyrochlore structure. Figure 9(c) shows nature of further distortion in the pyrochlore

structure below T_{FE2} . These results demonstrate successive distortions in the pyrochlore structure, corresponding to the successive ferroelectric transitions.

Our comprehensive investigation into the structural and ferroelectric characteristics of frustrated pyrochlore compounds, particularly focusing on both the pristine and V-doped STO, has provided rich insights into the interplay between magnetic frustration and ferroelectric order. We have uncovered distinct ferroelectric phases in both compounds, manifesting around temperatures of ~ 182 K (T_{FE1}) and ~ 52 K (T_{FE2}). Remarkably, these ferroelectric transitions occur in the absence of long-range magnetic ordering, suggesting that the emergence of ferroelectricity is primarily driven by factors beyond conventional magnetic interactions. The introduction of V dopants has revealed intriguing effects on the ferroelectric properties, as evidenced by the observed reduction in polarization values. This reduction may be correlated with the structural disorder in STVO caused by V doping. Additionally, the identification of a novel short-range magnetic ordering around 272 K exclusively in the V-doped compound underscores the intricate interplay between magnetic dopants and frustrated pyrochlore structure of the system. As highlighted in Fig. 1, the direct Sm–Sm distance in the pyrochlore structure and the V/Ti–Sm distance are exactly the same in the $Fd\bar{3}m$ structure, indicating comparable exchange coupling due to V doping. Therefore, V doping introduces a significant perturbation to the frustrated pyrochlore systems, strongly influencing the ME coupling as well as the polarization value. The occurrence of ME coupling without long-range magnetic order promising for developing ME materials, which can be further enhanced by doping with magnetic elements. Looking ahead, future research endeavors could delve deeper into elucidating the underlying mechanisms governing ME coupling in frustrated pyrochlore compounds, especially without long-range magnetic order.

To conclude, two ferroelectric orders are revealed well above the dipolar-octupolar antiferromagnetic ordering for STO. A structural transition around 182 K to a polar $R3m$ phase from the high-temperature $Fd\bar{3}m$ space group is associated with the occurrence of higher-temperature ferroelectric ordering. The frustrated pyrochlore structure formed by the Sm atoms is correlated with the ferroelectric order, where the release of magnetic frustration drives a distortion in the pyrochlore structure within the $R3m$ space group, suggesting a correlation with the emergence of ferroelectric order. The replacement of non-magnetic Ti by magnetic V^{4+} strongly influences the ferroelectric polarization as well as the ME coupling in STVO. The value of ferroelectric polarization decreases, while the ME coupling is enhanced due to V doping in STO. The emergence of ME coupling without the involvement of long-range magnetic order is unusual and is further enhanced by V doping. This observation indicates a new pathway for tuning ME coupling.

Acknowledgment

S.G. would like to thank BRNS, India (No. 58/14/09/2023/11737), SERB, India, for the CRG project (No. CRG/2022/000718), and the Department of Science and Technology, India, for the financial support (Proposal No. ID-IB-2021-07), and Jawaharlal

Nehru Centre for Advanced Scientific Research, Bangalore, India for facilitating the experiments at the beamline P21.1, DESY Synchrotron Facility, Hamburg, Germany. S.G. also would like to acknowledge UGC-DAE Consortium for the instrumental support of scientific research (No. CRS/2022-23/01/685).

-
- [1] R. Moessner and A. R. Ramirez, Geometrical frustration, *Phys. Today* **59**, 24 (2006).
- [2] R. Moessner and J. T. Chalker, Properties of a classical spin liquid: the Heisenberg pyrochlore antiferromagnet, *Phys. Rev. Lett.* **80**, 2929 (1998).
- [3] O. Benton, L.D.C. Jaubert, H. Yan, and N. Shannon, A spin-liquid with pinch-line singularities on the pyrochlore lattice, *Nat. Commun.* **7**, 11572 (2016).
- [4] S. T. Bramwell, M. J. P. Gingras, Spin Ice State in Frustrated Magnetic Pyrochlore Materials, *Science* **294**, 1495 (2001).
- [5] L. Bovo, X. Moya, D. Prabhakaran, Y. A. Soh, A.T. Boothroyd, N.D. Mathur, G. Aeppli and S.T. Bramwell, Restoration of the third law in spin ice thin films. *Nat Commun* **5**, 3439 (2014).
- [6] A. P. Ramirez, A. Hayashi, R. J. Cava, R. Siddharthan, and B. S. Shastry, Zero-point entropy in ‘spin ice’, *Nature (London)* **399**, 333 (1999).
- [7] H. Shinaoka, Y. Tomita, and Y. Motome, Effect of magnetoelastic coupling on spin-glass behavior in Heisenberg pyrochlore antiferromagnets with bond disorder, *Phys. Rev. B* **90**, 165119 (2014).
- [8] K. Mitsumoto, C. Hotta, and H. Yoshino, Spin-orbital glass transition in a model of a frustrated pyrochlore magnet without quenched disorder *Phys. Rev. Lett.* **124**, 087201 (2020).
- [9] J. E. Greedan, Proceedings of Rare Earths’04, Nara, Jpn. *J. Alloys Compd.* **408**, 444 (2006).
- [10] J. A. M. Paddison, G. Ehlers, A. B. Cairns, J. S. Gardner, O. A. Petrenko, N. P. Butch, D. D. Khalyavin, P. Manuel, H. E. Fischer, H. Zhou, A. L. Goodwin, and J. R. Stewart, Suppressed-moment 2-K order in the canonical frustrated antiferromagnet $Gd_2Ti_2O_7$, *npj Quantum Materials* **6**, 99 (2021).
- [11] O. A. Petrenko, M. R. Lees, G. Balakrishnan, V. N. Glazkov, and S. S. Sosin, Magnetic phases in a $Gd_2Ti_2O_7$ pyrochlore for a field applied along the [100] axis, *Phys. Rev. B* **85**, 180412(R) (2012).
- [12] M. J. P. Gingras, B. C. den Hertog, M. Faucher, J. S. Gardner, S.R. Dunsiger, L. J. Chang, B. D. Gaulin, N. P. Raju, and J. E. Greedan, Thermodynamic and single-ion properties of Tb^{3+} within the collective paramagnetic-spin liquid state of the frustrated pyrochlore antiferromagnet $Tb_2Ti_2O_7$, *Phys. Rev. B* **62**, 6496 (2000).
- [13] J. S. Gardner, A. Keren, G. Ehlers, C. Stock, E. Segal, J. M. Roper, B. Fak, M. B. Stone, P. R. Hammar, D. H. Reich, and B. D. Gaulin, Dynamic frustrated magnetism in $Tb_2Ti_2O_7$ at 50 mK, *Phys. Rev. B* **68**, 180401(R) (2003).
- [14] M. E. Zhitomirsky, M. V. Gvozdikova, P. C. W. Holdsworth, and R. Moessner, Quantum order by disorder and accidental soft mode in $Er_2Ti_2O_7$, *Phys. Rev. Lett.* **109**, 077204 (2012).
- [15] A. K. R. Briffa, R. J. Mason, and M. W. Long, Magnetic structure of $Er_2Ti_2O_7$, *Phys. Rev. B* **84**, 094427 (2011).
- [16] A. M. Samarakoon, K. Barros, Y. W. Li, M. Eisenbach, Q. Zhang, F. Ye, V. Sharma, Z. L. Dun, H. Zhou, S. A. Grigera, C. D. Batista, and D. A. Tennant, Machine-learning-assisted insight into spin ice $Dy_2Ti_2O_7$, *Nat. Commun.* **11**, 892 (2020).
- [17] E. R. Kassner, A. B. Eyvazov, B. Pichler, and J. C. Séamus Davis, Supercooled spin liquid state in the frustrated pyrochlore $Dy_2Ti_2O_7$, *PNAS* **112**, 8549 (2015).
- [18] T. Fennell, P. P. Deen, A. R. Wildes, K. Schmalzl, D. Prabhakaran, A. T. Boothroyd, R. J. Aldus, D. F. McMorrow, and S. T. Bramwell, Magnetic coulomb phase in the spin ice $Ho_2Ti_2O_7$, *Science*, **326**, 415-417 (2009).
- [19] R. A. Borzi, F. A. Gómez Albarracín, H. D. Rosales, G. L. Rossini, A. Steppke, D. Prabhakaran, A. P. Mackenzie, D. C. Cabra, and S. A. Grigera, Intermediate magnetization state and competing orders in $Dy_2Ti_2O_7$ and $Ho_2Ti_2O_7$, *Nat. Commun.* **7**, 12592 (2016).
- [20] M.J. Harris, S.T. Bramwell, D.F. McMorrow, T. Zeiske, and K.W. Godfrey, Geometrical Frustration in the Ferromagnetic Pyrochlore $Ho_2Ti_2O_7$, *Phys. Rev. Lett.* **79**, 2554 (1997).
- [21] E. Kermarrec, J. Gaudet, K. Fritsch, R. Khasanov, Z. Guguchia, C. Ritter, K. A. Ross, H. A. Dabkowska, and B. D. Gaulin, Ground state selection under pressure in the quantum pyrochlore magnet $Yb_2Ti_2O_7$, *Nat. Commun.* **8**, 14810 (2017).
- [22] A. Scheie, J. Kindervater, S. Zhang, and C. Broholm, Multiphase magnetism in $Yb_2Ti_2O_7$, *PNAS* **117**, 27245-27254 (2020).
- [23] C. Mauws, A. M. Hallas, G. Sala, A. A. Aczel, P. M. Sarte, J. Gaudet, D. Ziat, J. A. Quilliam, J. A. Lussier, M. Bieringer, H. D. Zhou, A. Wildes, M. B. Stone, D. Abernathy, G. M. Luke, B. D. Gaulin, and C. R. Wiebe, Dipolar-octupolar Ising antiferromagnetism in $Sm_2Ti_2O_7$: A moment fragmentation candidate, *Phys. Rev. B* **98**, 100401(R) (2018).
- [24] O. Benton, Ground-state phase diagram of dipolar-octupolar pyrochlores, *Phy. Rev. B* **102**, 104408 (2020).
- [25] S. Singh, S. Saha, S. K. Dhar, R. Suryanarayanan, A. K. Sood, and A. Revcolevschi, Manifestation of geometric frustration on magnetic and thermodynamic properties of the pyrochlores $Sm_2X_2O_7$ ($X=Ti,Zr$), *Phys. Rev. B* **77**, 054408 (2008).
- [26] J. M. Farmer, L. A. Boatner, B. C. Chakoumakos, M.-H. Du, M. J. Lance, C. J. Rawn, and J. C. Bryan, Structural and crystal chemical properties of rare-earth titanate pyrochlores, *J. Alloys Compounds* **605**, 63 (2014).
- [27] M. N. Valdeza, N. A. Spaldin, Origin and evolution of ferroelectricity in the layered rare-earth-titanate, $R_2Ti_2O_7$, Carpy-Galy phases, *Polyhedron* **171**, 181 (2019).
- [28] S. J. Patwe, V. Katari, N. P. Salke, S. K. Deshpande,

- R. Rao, M. K. Gupta, R. Mittal, S. N. Achary and A. K. Tyagi, Structural and electrical properties of layered perovskite type $\text{Pr}_2\text{Ti}_2\text{O}_7$: experimental and theoretical investigations, *J. Mater. Chem. C*, **3**, 4570 (2015)
- [29] S. Nanamatsu, M. Kimura, K. Doi, S. Matsushita and N. Yamada, A new ferroelectric: $\text{La}_2\text{Ti}_2\text{O}_7$, *Ferroelectrics* **8**, 511 (1914).
- [30] Z. Shao, S. Saitzek, A. Ferri, M. Rguiti, L. Dupont, P. Roussel, R. Desfeux, Evidence of ferroelectricity in metastable $\text{Sm}_2\text{Ti}_2\text{O}_7$ thin film, *J. Mater. Chem.*, **22**, 9806 (2012).
- [31] S. Saitzek, Z. Shao, A. Bayart, A. Ferri, M. Huve, P. Roussel and R. Desfeux, Ferroelectricity in $\text{La}_2\text{Zr}_2\text{O}_7$ thin films with a frustrated pyrochlore-type structure, *J. Mater. Chem. C* **2**, 4037 (2014).
- [32] Y. Tabira, R. L. Withers, L. Minervini, and R. W. Grimes, Systematic structural change in selected rare earth oxide pyrochlores as determined by wide-angle CBED and a comparison with the results of atomistic computer simulation, *J. Solid State Chem.* **153**, 16 (2000).
- [33] C. De, S. Ghara and A. Sundaresan, Effect of internal electric field on ferroelectric polarization in multiferroic TbMnO_3 , *Solid State Commun.* **205**, 61 (2015).
- [34] S. Mukherjee, G. Manna, P. Saha, S. Majumdar and S. Giri, Ferroelectric order with a linear high-field magnetoelectric coupling in $\text{Na}_2\text{Co}_2\text{TeO}_6$: A proposed Kitaev compound, *Phys. Rev. Mater.* **6**, 054407 (2022).
- [35] A. Rakshit, Transition metal oxide-based devices for memory applications, [Doctoral dissertation, Technion - Israel Institute of Technology, 2020].
- [36] N. Terada, Y. S. Glazkova, and A. A. Belik, Differentiation between ferroelectricity and thermally stimulated current in pyrocurrent measurements of multiferroic $\text{M Mn}_7\text{O}_{12}$ ($\text{M} = \text{Ca}, \text{Sr}, \text{Cd}, \text{Pb}$), *Phys. Rev. B* **93**, 155127 (2016).
- [37] S. Mukherjee, N. Mondal, M. Polentarutti, G. Bais, S. Majumdar, and S. Giri, Linear magnetoelectric coupling without long-range magnetic order and rare-earth-free large magnetocaloric effect in $\text{Co}_3\text{V}_2\text{O}_8$, *Phys. Rev. B* **109**, 014418 (2024).
- [38] A. Karmakar, K. Dey, S. Chatterjee, S. Majumdar, and S. Giri, Spin correlated dielectric memory and rejuvenation in multiferroic CuCrS_2 , *Appl. Phys. Lett.* **104**, 052906 (2014).
- [39] J. K. Dey, A. Chatterjee, S. Majumdar, A. C. Dippel, O. Gutowski, M. v. Zimmermann, and S. Giri, Ferroelectric order associated with ordered occupancy at the octahedral site of the inverse spinel structure of multiferroic NiFe_2O_4 , *Phys. Rev. B* **99**, 144412 (2019).
- [40] A. Pal, T. W. Yen, T. W. Kuo, C. W. Wang, S. M. Huang, M. C. Chou, Y. C. Lai, Y. C. Chuang, P. Yanda, A. Sundaresan, H. S. Kunwar, V. G. Sathe, A. Tiwari, D. C. Kakarla and H. D. Yang, Unconventional multiferroicity induced by structural distortion and magnetostriction effect in the layered spin-1/2 ferrimagnet $\text{Bi}_2\text{Cu}_5\text{B}_4\text{O}_{14}$, *Phys. Rev. B* **107**, 184430 (2023).
- [41] A. Chatterjee, J. K. Dey, S. Majumdar, A. -C. Dippel, O. Gutowski, M. v. Zimmermann, S. Giri, Tuning of multiferroic order with Co doping in CuCr_2O_4 : Interplay between structure and orbital order, *Phys. Rev. Materials* **3**, 104403 (2019).
- [42] E. V. Ramana, F. Figueiras, A. Mahajan, D. M. Tobaldi, B. F. O. Costa, M. P. F. Graça, and M. A. Valente, Effect of Fe-doping on the structure and magnetoelectric properties of $(\text{Ba}_{0.85}\text{Ca}_{0.15})(\text{Ti}_{0.9}\text{Zr}_{0.1})\text{O}_3$ synthesized by a chemical route, *J. Mater. Chem. C* **4**, 1066 (2016).
- [43] I. E. Dzyaloshinskii, The magneto-electrical effect in antiferromagnets, *Sov. Phys. JETP* **10**, 628 (1960).
- [44] D. N. Astrov, The magnetoelectric effect in antiferromagnetics, *Sov. Phys. JETP* **11**, 708 (1960).
- [45] E. Fogh, B. Klemke, M. Reehuis, P. Bourges, C. Niedermayer, S. H.-Dahlin, O. Zaharko, J. Schefer, A. B. Kristensen, M. K. Sorensen, S. Paeckel, K. S. Pedersen, R. E. Hansen, A. Pages, K. K. Moerner, G. Meucci, J.-R. Soh, A. Bombardi, D. Vaknin, H. M. Ronnow, O. F. Syljuasen, N. B. Christensen and R. T.-Petersen, Tuning magnetoelectricity in a mixed anisotropy antiferromagnet, *Nat. Comm.* **14**, 3408 (2023).
- [46] A. Hati, S. Mukherjee, N. Mondal, S. Bhowmik, G. Manna, S. Majumdar, and S. Giri, Multiferroic order and large magnetic refrigeration capacity in $\text{Gd}_2\text{MnFeO}_6$: Significance of magnetic frustration and Jahn-Teller distortion, *Phys. Rev. B* **108**, 144431 (2023).
- [47] K. Dey, A. Karmakar, A. Indra, S. Majumdar, U. Rütt, O. Gutowski, M. v. Zimmermann, and S. Giri, Thermally assisted and magnetic field driven isostructural distortion of spinel structure and occurrence of polar order in CoCr_2S_4 , *Phys. Rev. B* **92**, 024401 (2015).
- [48] K. Dey, S. Majumdar, and S. Giri, Ferroelectricity in spiral short-range-ordered magnetic state of spinel MnCr_2O_4 : Significance of topological frustration and magnetoelastic coupling, *Phys. Rev. B* **90**, 184424 (2014).
- [49] A. Indra, K. Dey, S. Majumdar, I. Sarkar, S. Francoual, R. P. Giri, N. Khan, P. Mandal, and S. Giri, Magnetoelectric memory in reentrant frozen state and considerable ferroelectricity in the multiferroic spin-chain compound $\text{Sm}_2\text{BaNiO}_5$, *Phys. Rev. B* **95**, 094402 (2017).
- [50] A. Indra, K. Dey, J. K. Dey, S. Majumdar, U. Rütt, O. Gutowski, M. v. Zimmermann, and S. Giri, CrO_4 distortion-driven ferroelectric order in $(\text{R}, \text{Y})\text{CrO}_4$ ($\text{R} = \text{Sm}, \text{Gd}, \text{and Ho}$): A new family of multiferroics, *Phys. Rev. B* **98**, 014408 (2018).
- [51] J. K. Dey, A. Chatterjee, A.-C. Dippel, O. Gutowski, M. v. Zimmermann, S. Majumdar, and S. Giri, Rhombohedral distortion-driven ferroelectric order and exchange bias effect in geometrically frustrated ZnFe_2O_4 , *Phys. Rev. Mater.* **5**, 014410 (2021).
- [52] B. J. Campbell, H. T. Stokes, D. E. Tanner, and D. M. Hatch, ISODISPLACE: a web-based tool for exploring structural distortions, *J. Appl. Crystallogr.* **39**, 607 (2006).
- [53] V. Caignaert, A. Maignan, K. Singh, Ch. Simon, V. Pralong, B. Raveau, J. F. Mitchell, H. Zheng, A. Huq, and L. C. Chapon, Gigantic magnetic-field-induced polarization and magnetoelectric coupling in a ferrimagnetic oxide $\text{CaBaCo}_4\text{O}_7$, *Phys. Rev. B* **88**, 174403 (2013).
- [54] K. Dey, A. Indra, A. Chatterjee, S. Majumdar, U. Rütt, O. Gutowski, M. v. Zimmermann, and S. Giri, Chemical-pressure-driven orthorhombic distortion and significant enhancement of ferroelectric polarization in $\text{Ca}_{1-x}\text{La}_x\text{BaCo}_4\text{O}_7$ ($x \leq 0.05$), *Phys. Rev. B* **96**, 184428 (2017).
- [55] F. Kubel and H. Schmid, Structure of a ferroelectric and ferroelastic monodomain crystal of the perovskite BiFeO_3 , *Acta Crystallogr.* **B46**, 698 (1990).
- [56] J.-G. Park, M. D. Le, J. Jeong, and S. Lee, Structure and

spin dynamics of multiferroic BiFeO_3 , *J. Phys.: Condens. Matter* **26**, 433202 (2014).